Negative Magnus Effect on a Rotating Sphere at around the Critical Reynolds Number

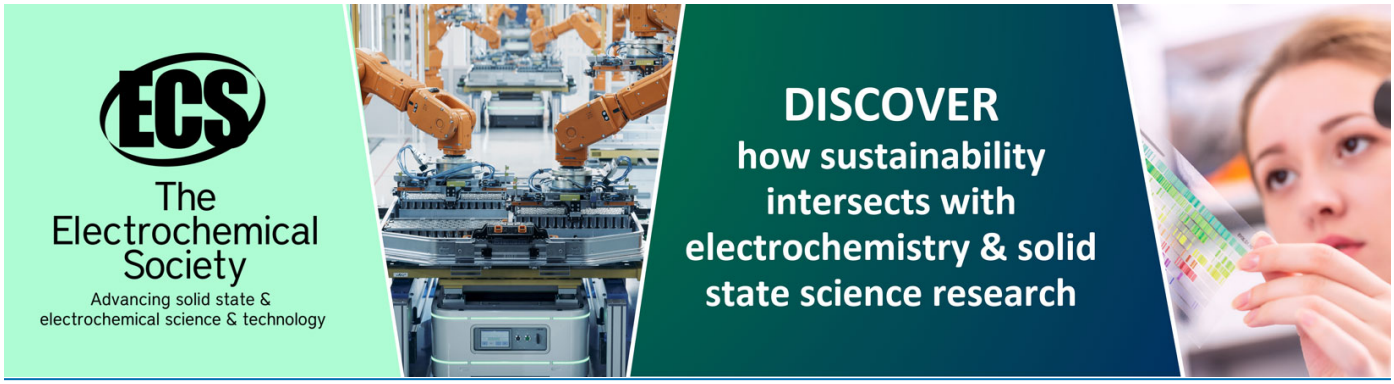

Journal of Physics: Conference Series **318** (2011) 032021 doi:10.1088/1742-6596/318/3/032021

Negative Magnus Effect on a Rotating Sphere at around the Critical Reynolds Number

Masaya MUTO[1], Hiroaki WATANABE[1], Makoto TSUBOKURA[2] & Nobuyuki OSHIMA[2]

[1]High Efficiency Power Generation Sector, Energy Engineering Research Laboratory, Central Research Institute of Electric Power Industry, 2-6-1, Nagasaka, Yokosuka, Kanagawa 240-0196, Japan

[2]Division of Mechanical and Space Engineering, Faculty of Engineering, Hokkaido University, N13W8, Kita-ku, Sapporo, Hokkaido 060-8628, Japan

E-mail: mtsubo@eng.hokudai.ac.jp

Abstract. Negative Magnus lift acting on a sphere rotating about the axis perpendicular to an incoming flow is investigated using large-eddy simulation at three Reynolds numbers of 1.0×10^4, 2.0×10^5, and 1.14×10^6. The numerical methods adopted are first validated on a non-rotating sphere and the spatial resolution around the sphere is determined so as to reproduce the laminar separation, reattachment, and turbulent transition of the boundary layer observed at around the critical Reynolds number. In the rotating sphere, positive or negative Magnus effect is observed depending on the Reynolds number and the rotating speed imposed. At the Reynolds number in the subcritical or supercritical region, the direction of the lift force follows the Magnus effect to be independent of the rotational speed tested here. In contrast, negative lift is observed at the Reynolds number at the critical region when particular rotating speeds are imposed. The negative Magnus effect is discussed in the context of the suppression or promotion of boundary layer transition around the separation point.

1. Introduction

The Magnus effect is the phenomenon by which a clockwise-rotating sphere or cylinder subjected to a left-to-right flow experiences a lift force (Magnus, 1853). While the mechanism is usually explained in terms of the inviscid flow, the same phenomenon is also applied to explain the curious and unpredictable motions of spinning balls used in sports such as baseball, volleyball, and football. The phenomenon becomes complicated by viscous effects in the flow as the boundary layer on the surface of the ball separates due to an adverse pressure gradient. Generally, the difference in the relative velocity of the sphere surface with respect to the incoming uniform flow makes the boundary layer on the forward-moving side (upper side in this context) thinner than that on the backward-moving side. Thus, the boundary-layer separation is delayed on the forward-moving side, while it is accelerated on the backward-moving side. As a result, the wake flow is distorted downward, and a positive lift force acts on the sphere based on the principle of action and reaction. In addition, the laminar-turbulent transition of the boundary layer complicates the phenomenon even more, as it causes the separation point to shift considerably downstream along the surface. Thus, the drag of the non-rotating sphere substantially decreases around the critical Reynolds number. As a result of the interaction of these separation and

transition phases, some experimental studies have reported a negative lift force on a rotating sphere, which contradicts the Magnus effect, at some specific rotational speed around the critical Reynolds number (Maccoll, 1928; Davies, 1949; Taneda, 1957). However, at the same time, it is indeed difficult to measure the minute positive or negative lift force on the rotating sphere in experiments without the influence of supporting rods or wires. The difficulty appears as a quantitative disagreement among the existing experimental data regarding the magnitude of the lift force, the Reynolds-number range, or the rotational speed where the negative Magnus effect is observed. Hence, little knowledge has so far been obtained concerning the mechanism of the negative Magnus effect. Subsequently, the objectives of this study are to investigate characteristics of the boundary layer when the negative Magnus lift occurs on a rotating by using a numerical simulation.

2. Numerical Methods

2.1. Computational domain and boundary conditions

The computational domain consisted of a rectangular duct and the sphere was fixed in the center of the domain as shown in Fig. 1. Thirty prism-mesh layers were inserted on the sphere surface to resolve the velocity profile of the boundary layer. The spatial resolution around the sphere was determined so as to reproduce the drag reduction at the critical Reynolds number. The other region of the domain was divided by tetrahedral grids except for several prism layers on the inlet, outlet, and sidewall boundaries. An overview of the spatial resolution near the sphere at each Reynolds number is shown in Fig. 2. A no-slip boundary condition was adopted on the sphere surface and the clockwise rotation of the sphere was represented by a rotating velocity distribution on the surface. A uniform velocity profile without any perturbation was imposed as the inlet boundary condition. The gradient-free condition for the pressure and velocity was applied to the duct outlet. The difficulty of the numerical treatment on the target flow lies in the fact that the grid resolution in the vicinity of the surface should be fine enough for the normal surface direction to capture the boundary-layer distortion during the separation phenomena. In addition, the grid allocation should be homogeneous along the flow direction to properly capture the transition to turbulence. Thus, the spherical or cylindrical coordinate (Constantinescu & Squires, 2004; G. Yun & Choi, 2006) was avoided, and instead, an unstructured finite volume grid was adopted. For that reason, if we assume an incompressible Newtonian flow, the continuity and the Navier-Stokes equations were discretized based on the vertex-centered finite volume method.

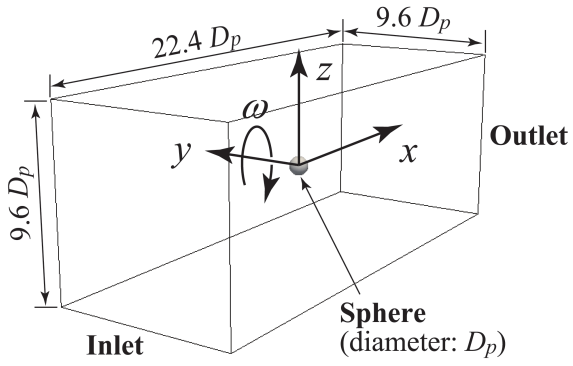

Figure 1. Coordinate system and geometry of computational domain.

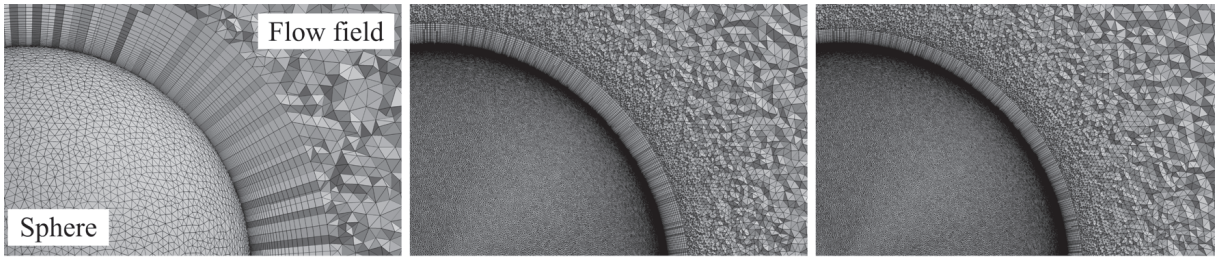

Figure 2. Spatial resolution of numerical grids allocated around the sphere: (a)Re_p=1.0×10^4; (b)Re_p=2.0×10^5; (c)Re_p=1.14×10^6.

2.2. Numerical conditions

The non-dimensional rotational speed, or more conventionally called the spin parameter, is defined as the ratio of the circumferential velocity to the incoming flow velocity as $\Gamma = D_p\omega/U_0$, in which D_p is the sphere diameter, ω is the rotating angular velocity, and U_0 is the incoming flow velocity. According to previous experimental studies, the negative Magnus effect was observed at a Γ less than 0.5. Thus, two non-dimensional velocities of $\Gamma = 0.2$ and 1 were considered in this study. On the other hand, as noted above, a relatively large discrepancy was acknowledged concerning the Reynolds number at which the negative lift was observed (Maccoll, 1928; Davies, 1949). As the Reynolds numbers $Re_p = U_0 D_p/\nu$ (ν is the kinetic viscosity), 1.0×10^4, 2.0×10^5, and 1.14×10^6 in the subcritical, critical, and supercritical flow ranges (Achenbach, 1972), respectively, were considered. To investigate the high Reynolds-number turbulent flow including transition, large-eddy simulation (LES) with a dynamic subgrid-scale model was adopted as a numerical method.

2.3. Validation of methods

The numerical schemes and grids described in the previous section were first validated on the flow around a non-rotating sphere. Fig. 3 plots the drag coefficient profiles obtained for each Reynolds-number condition, in which experimental data (Achenbach, 1972; Schlichting, 1955; Wieselsberger, 1922) are also shown for reference. In addition to the three Reynolds numbers indicated in previous section, two additional Reynolds-number conditions of $Re_p = 1.6 \times 10^5$ and 2.4×10^5 were also used to see whether our numerical method properly reproduces the drag crisis in the critical flow range, in which we used the same numerical grids as for $Re_p = 2.0 \times 10^5$. The drag coefficient C_D is defined as $C_D = F_D/(\frac{1}{2}\rho U_0^2 A)$, where F_D, ρ, and A are the drag force, fluid density, and the projected area of the sphere, respectively. The drag crisis phenomena in which the drag substantially decreases as the Reynolds number increases from 1×10^5 to 3×10^5 is remarkable, while quantitative disagreement among the three experimental data parts is not negligible. The critical Reynolds number $Re_p = 3.7 \times 10^5$ observed by Achenbach (1972) is about twice that of Wieselsberger (1922). Our numerical results qualitatively reproduce the drag crisis and show good agreement with those measured by Wieselsberger (1922). From these results, we can say that our simulation properly captured the flow characteristics around the critical Reynolds number.

2.4. An effect of the rotating speed on the lift coefficient

Fig. 4 shows the time-averaged velocity magnitude and the pressure distribution on the sphere surface for three Reynolds numbers and $\Gamma = 0.2$. The positive lift of the sphere is verified by the distorted wake for the downward direction in the case of the conventional Magnus effect

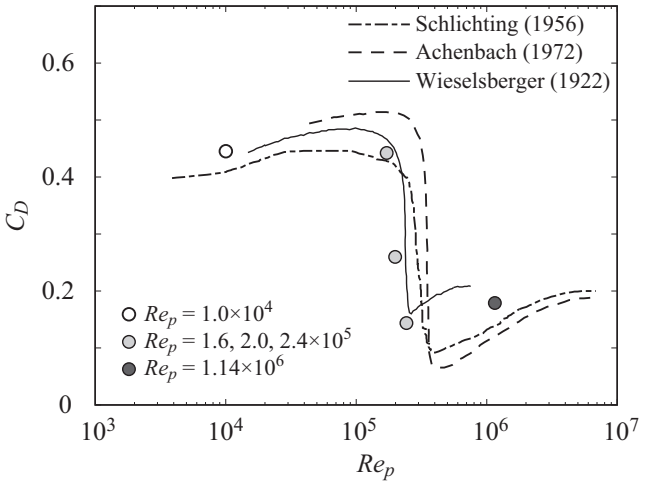

Figure 3. Drag coefficient as a function of the Reynolds number in subcritical, critical and supercritical flow range.

($Re_p = 1.0 \times 10^4$ and $\Gamma = 0.2$). On the other hand, when negative Magnus force is observed ($Re_p = 2.0 \times 10^5$ and $\Gamma = 0.2$), the wake is inclined upward, suggesting the negative lift force acting on the sphere. In fact, contrary to the case with positive lift, the separation point of the boundary layer in the forward-moving side shifts downstream, while it is vice versa in the backward-moving side. As a result, the reverse flow region behind the separation point indicated by the blue region is wider in the forward-moving side, as shown in the figure. The negative Magnus effect disappears as Reynolds number increases ($Re_p = 1.14 \times 10^6$ and $\Gamma = 0.2$), the wake is inclined downward again.

To discuss the mechanism of the negative Magnus effect, the time-averaged pressure coefficient C_p distribution along the sphere surface experiencing the positive or negative lift are respectively plotted in the left and right graphs in figure 5. The experimental data of the still sphere at the subcritical and supercritical conditions, which correspond respectively to the laminar (Achenbach, 1972) and turbulent separation (Fage, 1936), are also plotted. According to the surface pressure distribution in the left graph in figure 5, the separation point in the forward-moving side shifts downstream, whereas the separation point in the backward-moving side shifts upstream, compared with the non-rotating case. Then the pressure distribution on the sphere becomes axisymmetric, causing the ordinary Magnus lift. The boundary layers on both sides of the sphere are considered to be in the laminar state, and no reattachment or reseparation is identified at this smaller Reynolds number. In contrast, in the center graph in figure 5, it is acknowledged that the profile on the forward-moving side deviates from the case without rotation and comes close to the one in the subcritical case. This result can be explained by the suppression of the turbulent transition caused by the decrease in the relative velocity in the boundary layer with respect to the incoming flow on the forward-moving side. Then the laminarized boundary layer separates slightly faster than the transient case, and the separation point shifts upstream. On the other hand, the separation bubble observed in the non-rotating case becomes smaller on the backward-moving side, and the profile comes close to the one in the supercritical case. It is reasonable to say that the relative velocity in the boundary layer increases because of the rotation, which promotes the turbulent transition at this region. Finally, at supercritical Reynolds number region shown in the right graph in figure 5, the pressure distribution becomes similar to the case of subcritical region and negative Magnus effect disappears.

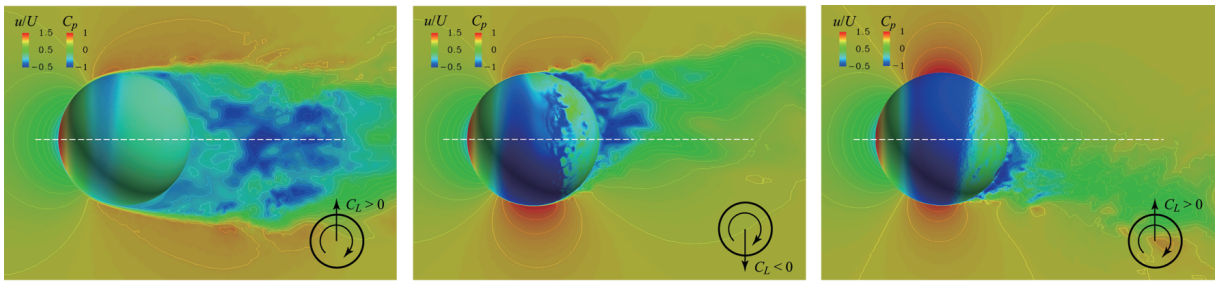

Figure 4. Contours of the instantaneous streamwise velocity on the central cross section and the static pressure coefficient on the sphere surface at $\Gamma = 0.2$: (a) $Re_p = 1.0 \times 10^4$; (b) $Re_p = 2.0 \times 10^5$; (c) $Re_p = 1.14 \times 10^6$.

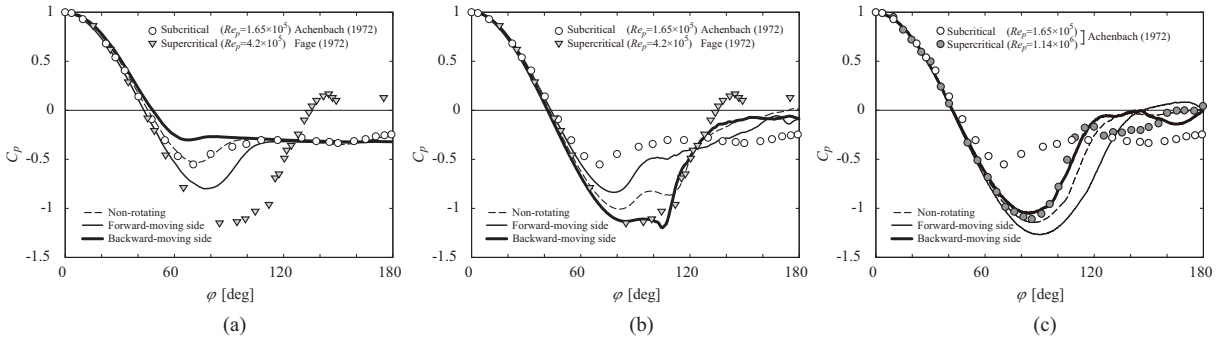

Figure 5. Time averaged pressure coefficient Cp distribution around drag crisis region with rotation at $\Gamma = 0.2$: (a) $Re_p = 1.0 \times 10^4$; (b) $Re_p = 2.0 \times 10^5$; (c) $Re_p = 1.14 \times 10^6$.

3. Visualization of boundary layer separation

3.1. Boundary layer transition with rotation

Fig. 6 to 8 show instantaneous vortical structures around the non-rotating and rotating sphere at the each Reynolds numbers. In those figures, vortical structure is obtained as an iso-surface of the second invariance of the velocity gradient tensor. In both non-rotating and rotating cases at $Re_p = 1.0 \times 10^4$ as shown in Fig. 6(a) to 6(c), we cannot identify remarkable structural vortex on the sphere surface compared to other Reynolds number cases. While at $Re_p = 2.0 \times 10^5$, in the non-rotating case as shown in Fig. 7(a), tubelike vortex structures are not identified around the first separation point (In this study, the first separation point of the boundary layer is determined as the streamwise velocity of the first nearest grid point from where the sphere surface becomes negative. In the same way, the reattachment point is identified when the velocity becomes positive again. Based on this definition, the separation point is located at $\phi = 87°$, $92°$, and $103°$ at $Re_p = 1.0 \times 10^4$, 2.0×10^5, and 1.14×10^6, respectively. Here, ϕ is the polar angle from the frontal stagnation point), suggesting that the separation is in the laminar state. On the other hand, the azimuthal tubelike vortex structures partially cover the sphere surface indicating that transition of the boundary layer occurs around the reattachment region. When the sphere rotates at $\Gamma = 0.2$ and the negative Magnus effect appears, as shown in Fig. 7(b), the boundary layer on the backward-moving side is perturbed around the first separation point and the laminar separation becomes indistinct. However, as Γ increases up to

1, the negative Magnus effect disappears because the relative velocity become close to zero on forward-moving side and separation is suppressed. In both non-rotating and rotating cases at $Re_p = 1.14 \times 10^6$ as shown in Fig. 8(a) to 8(c), vortex structures cover the sphere surface from around the first separation point suggesting that the boundary layer in both forward-moving side and backward-moving side sufficiently transit to turbulent state. Therefore the different state between forward-moving side and backward-moving side in boundary layer or separation seen in critical region number does not appear at $\Gamma = 0.2$.

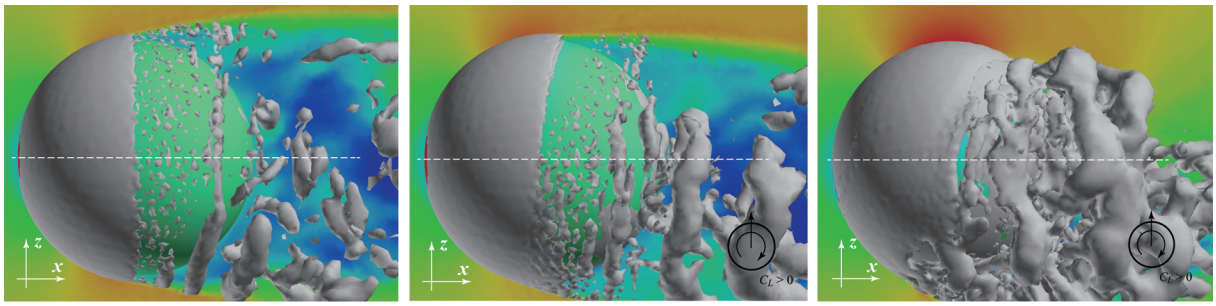

(a) (b) (c)

Figure 6. Contours of the streamwise velocity (x component) on the central cross section ($y = 0$) and the static pressure coefficient on the sphere surface with instantaneous vortical structures around the sphere (iso-surface of the second invariance of the velocity gradient tensor) at $Re_p = 1.0 \times 10^4$: (a) non-dimensional rotational speed $\Gamma = 0$; (b) $\Gamma = 0.2$; (c) $\Gamma = 1.0$.

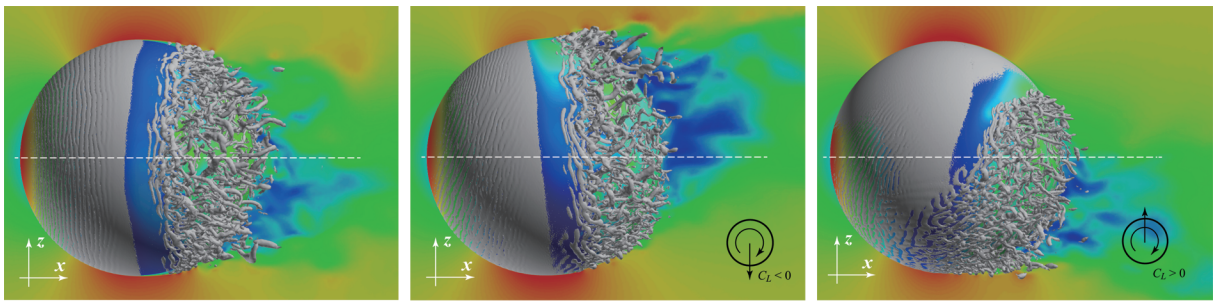

(a) (b) (c)

Figure 7. Contours of the streamwise velocity (x component) on the central cross section ($y = 0$) and the static pressure coefficient on the sphere surface with instantaneous vortical structures around the sphere (iso-surface of the second invariance of the velocity gradient tensor) at $Re_p = 2.0 \times 10^5$: (a) non-dimensional rotational speed $\Gamma = 0$; (b) $\Gamma = 0.2$; (c) $\Gamma = 1.0$.

3.2. Spatial distribution of separation point on the sphere surface

Figs. 10 to 12 show instantaneous iso-line of the zero-shear stress on the sphere surface for non-rotating and rotating cases at each Reynolds numbers. At $Re_p = 1.0 \times 10^4$ as shown in Fig. 10(a) to 10(c), iso-line is relatively smooth compared to other Reynolds number cases though the line shifts along with a rotation direction of the sphere in Fig. 10(b) and (c). While at $Re_p = 2.0 \times 10^5$, distribution of the iso-line in the rotating case at $\Gamma = 0.2$ as shown in Fig.

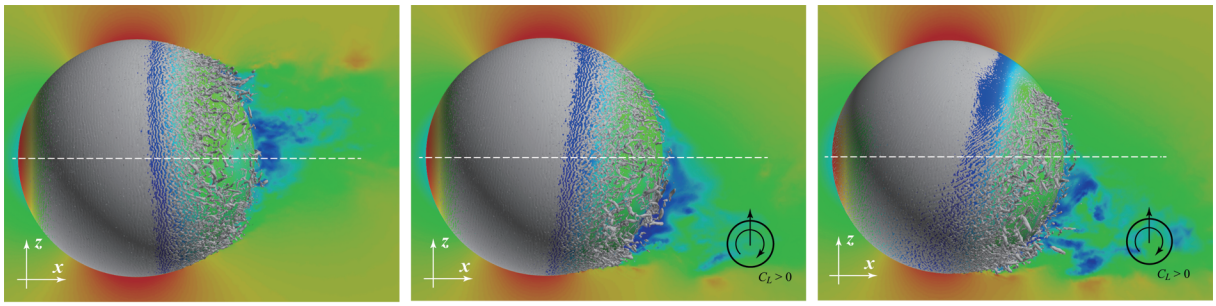

(a) (b) (c)

Figure 8. Contours of the streamwise velocity (x component) on the central cross section ($y = 0$) and the static pressure coefficient on the sphere surface with instantaneous vortical structures around the sphere (iso-surface of the second invariance of the velocity gradient tensor) at $Re_p = 1.14 \times 10^6$: (a) non-dimensional rotational speed $\Gamma = 0$; (b) $\Gamma = 0.2$; (c) $\Gamma = 1.0$.

11(b) shows that by rotation the iso-line shapes small discrete regions on the backward-moving side that indicates the boundary layer transition occurs on the side and the velocity distribution is more perturbed compared to the non-rotating case as shown in Fig. 11(a). When Γ increases up to 1, the iso-line in the forward-moving side becomes smooth due to a reduce of relative velocity between uniform flow and the sphere surface. Finally at $Re_p = 1.14 \times 10^6$ as shown in Fig. 12(a) to 12(c), the iso-line is no more smooth and shapes small regions on both backward and forward-moving side of the sphere not depending on the rotation. This is because the boundary layer on the sphere is fully transit to turbulent state.

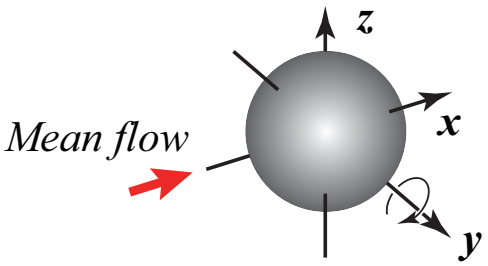

Figure 9. Coordinate system and rotating direction for Figures 10, 11 and 12.

4. Summary

Numerical simulation on the flow field around a rotating sphere was conducted by large-eddy simulation. Unsteady characteristics of the boundary layer is visualized at $Re_p = 1.0 \times 10^4$, 2.0×10^5, and 1.14×10^6 and the physical mechanism leading to the generation of negative Magnus lift was discussed in the context of the suppression or promotion of the boundary layer transition. In summary, the following results were obtained:

- In the critical flow range at $Re_p = 2.0 \times 10^5$, spatial fluctuation of velocity field generated from much upstream on the backward-moving side compared to forward-moving side. That causes spatially perturbed distribution of zero-shear iso-line on the backward-moving side.
- In the subcritical flow range at $Re_p = 1.0 \times 10^4$ in which the surface boundary layer is subjected to fully laminar separation, zero-shear iso-line is distributed smoothly on both the backward- and forward-moving side.

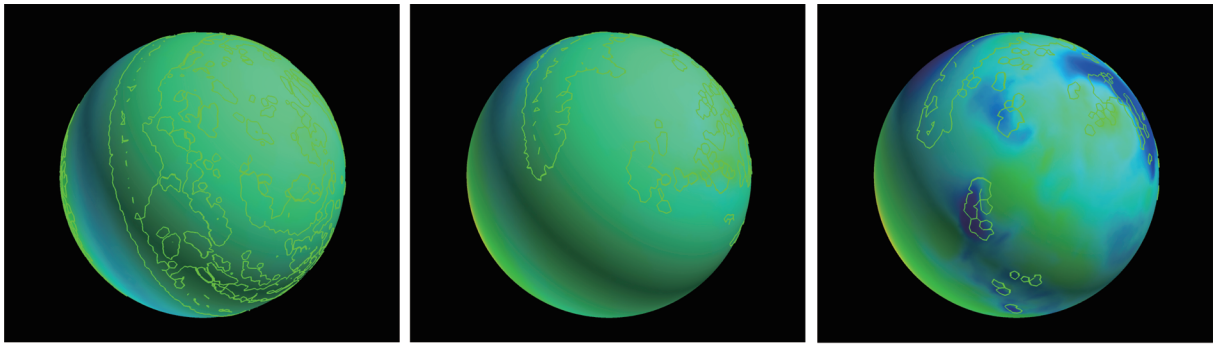

(a) (b) (c)

Figure 10. Instantaneous static pressure coefficient on the sphere surface and the iso-line of the zero-shear stress on the sphere surface at $Re_p = 1.0 \times 10^4$: (a) non-dimensional rotational speed $\Gamma = 0$; (b) $\Gamma = 0.2$, (c) $\Gamma = 1.0$.

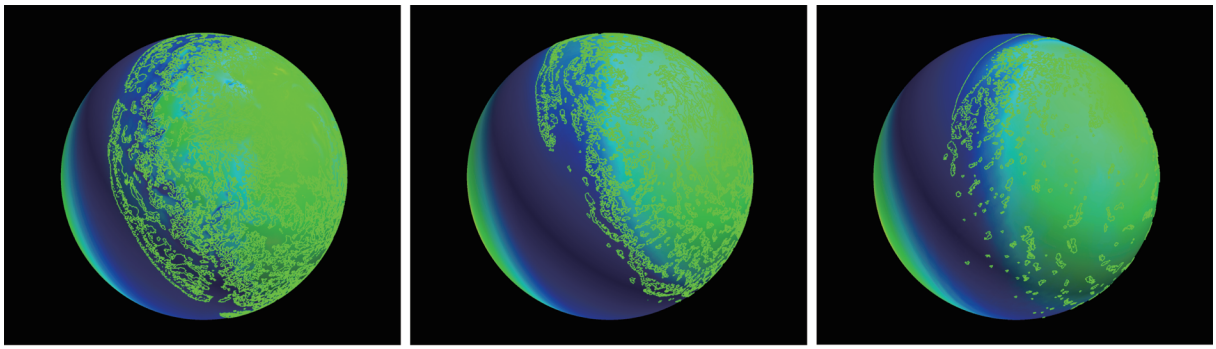

(a) (b) (c)

Figure 11. Instantaneous static pressure coefficient on the sphere surface and the iso-line of the zero-shear stress on the sphere surface at $Re_p = 2.0 \times 10^5$: (a) non-dimensional rotational speed $\Gamma = 0$; (b) $\Gamma = 0.2$, (c) $\Gamma = 1.0$.

- Finally, in the supercritical flow range at $Re_p = 1.14 \times 10^6$ in which the surface boundary layer is subjected to fully turbulent separation, zero-shear iso-line is not distributed smoothly not depending on the sphere rotational speed. And the lift force on the sphere monotonically increases as the rotational speed increases.

Acknowledgments

The authors acknowledge the support of the Ministry of Education, Culture, Sports, Science and Technology, Japan, in funding this study with a Grant-in-Aid for Scientific Research (C) 20560143. Also we are grateful to Mr. Tadashi Yamazaki for his valuable cooperation in our visualization of numerical results.

References

ACHENBACH, E. 1972 Experiments on the flow past spheres at very high reynolds numbers.

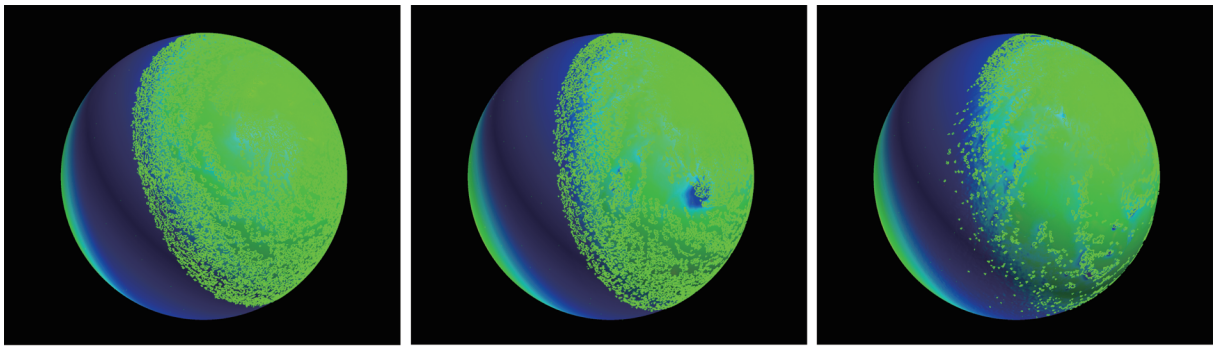

Figure 12. Instantaneous static pressure coefficient on the sphere surface and the iso-line of the zero-shear stress on the sphere surface at $Re_p = 1.14 \times 10^6$: (a) non-dimensional rotational speed $\Gamma = 0$; (b) $\Gamma = 0.2$, (c) $\Gamma = 1.0$.

Journal of Fluid Mechanics **54**, 565–575.

Constantinescu, G. & Squires, K. 2004 Numerical investigations of flow over a sphere in the subcritical and supercritical regimes. *Physics of Fluids* **16**, 1449–1466.

Davies, J. M. 1949 Aerodynamics of golf balls. *Journal od Applied Physics* **20**, 821–828.

Fage, A. 1936 Experiments on a sphere at critical reynolds numbers. *Aeronautical Research Council, Reports and Memoranda* 1766.

G. Yun, D. Kim & Choi, H. 2006 Vortical structures behind a sphere at subcritical reynolds numbers. *Physics of Fluids* **18**, 015102.

Maccoll, J. W. 1928 Aerodynamics of a spinning sphere. *Journal of the Royal Aeronautical Society* **28**, 777–798.

Magnus, G. 1853 Über die abweichung der geschosse, und: Über eine abfallende erscheinung bei rotierenden körpern. *Poggendorff's Annalen der Physik und Chemie* **164**, 1–29.

Schlichting, H. 1955 *Boudary Layer Theory*. UU.

Taneda, S. 1957 Negative magnus effect. *Report of Research Institute for Applied Mechanics* **5**, 123–128.

Wieselsberger, C. 1922 Weitere feststellungen uber die gesetze des flussigkeits und luftwiderstandes. *Physikalische Zeitschrift* **23**, 219–224.